ARTICLES

Linear and Nonlinear Spectroscopy of a Porphyrin−Squaraine−Porphyrin Conjugated System

Scott Webster,*,† Susan A. Odom,‡ Lazaro A. Padilha,† Olga V. Przhonska,†,§ Davorin Peceli,† Honghua Hu,† Gero Nootz,† Alexei D. Kachkovski,⊥ Jonathan Matichak,‡ Stephen Barlow,‡ Harry L. Anderson,¶ Seth R. Marder,‡ David J. Hagan,† and Eric W. Van Stryland†

CREOL, The College of Optics and Photonics, University of Central Florida, Orlando, Florida 32826, School of Chemistry and Biochemistry and Center for Organic Photonics and Electronics, Georgia Institute of Technology, Atlanta, Georgia 30332, Institute of Physics, National Academy of Sciences, Kiev, 03028, Ukraine, Institute of Organic Chemistry, National Academy of Sciences, Kiev, 03094, Ukraine, and Department of Chemistry, Chemistry Research Laboratory, University of Oxford, Oxford, OX1 3TA, U.K.

Received: May 13, 2009; Revised Manuscript Received: August 3, 2009

The linear and nonlinear absorption properties of a squaraine-bridged porphyrin dimer (POR-SQU-POR) are investigated using femto-, pico-, and nanosecond pulses to understand intramolecular processes, obtain molecular optical parameters, and perform modeling of the excited-state dynamics. The optical behavior of POR-SQU-POR is compared with its separate porphyrin and squaraine constituent moieties. Linear spectroscopic studies include absorption, fluorescence, excitation and emission anisotropy, and quantum yield measurements. Nonlinear spectroscopic studies are performed across a wide range (∼150 fs, ∼25 ps, and ∼5 ns) of pulsewidths and include two-photon absorption (2PA), single and double pump−probe, and Z-scan measurements with detailed analysis of excited-state absorption induced by both one- and two-photon absorption processes. The 2PA from the constituent moieties shows relatively small 2PA cross sections; below 10 GM ($1\ \mathrm{GM} = 1 \times 10^{-50}\ \mathrm{cm}^4$ s/photon) for the porphyrin constituent and below 100 GM for the squaraine constituent except near their one-photon resonances. In stark contrast, the composite POR-SQU-POR molecule shows 2PA cross sections greater than 10^3 GM over most of the spectral range from 850 to 1600 nm (the minimum value being 780 GM at 1600 nm). The maximum value is ∼11 000 GM near the Nd:YAG laser wavelength of 1064 nm. This broad spectral range of large 2PA cross sections is unprecedented in any other molecular system and can be explained by intramolecular charge transfer. A theoretical quantum-chemical analysis in combination with different experimental techniques allows insight into the energy-level structure and origin of the nonlinear absorption behavior of POR-SQU-POR.

1. Introduction

Much effort has been invested in the design, synthesis, and optimization of dyes with large optical nonlinearities with the ultimate goal of understanding structure−property relations so that the linear and nonlinear optical properties can be tailored for various applications. Organic compounds that have attracted significant attention include porphyrins and their analogous macrocycles as well as linear polymethines and related structures, such as squaraines. In both classes, the linear and nonlinear optical (NLO) properties can be tailored via specific structural modifications. Metalloporphyrin molecules have been extensively studied due to their importance in sensitization of singlet oxygen in photodynamic therapy and, more recently, in optoelectronic applications. Many aspects of the optical and electronic properties of porphyrins are already well-understood; see, for example, refs 1−5.

Since the first observation of reverse saturable absorption (RSA) in tetraphenylporphyrins reported in 1985,[6] the NLO properties of porphyrins and related compounds have been intensively studied in relation to two-photon absorption (2PA),[7−10] nano- and picosecond nonlinear transmittance,[11] and singlet−singlet and triplet−triplet excited-state absorption.[12,13] It has been established that porphyrin monomers are typically characterized by small 2PA cross sections, $\delta_{2PA} < 100$ GM; therefore, many attempts have been made to enhance this value by modifying molecular structures from monomer to dimers[8] and arrayed systems[14,15] for several applications.[16,17] As discussed in ref 18, various strategies to increase 2PA in porphyrins include: elongation of the effective π-conjugation length, incorporation of π-conjugated bridges in symmetrical and asymmetrical configurations, and variation of the electron-donating and/or electron-accepting strength in the terminal groups. As a result, researchers have deliberately incorporated these strategies when designing meso-doubly linked nickel−porphyrin arrays with large 2PA, which have been found to exhibit δ_{2PA} values of up to ∼8000 GM/unit (a maximum of five units was synthesized with a total $\delta_{2PA} \sim 41\ 400$).[18] This tailored molecular design includes the following: (1) a long π-conjugated pathway over the whole array system; (2) increased strength of the donor and

* Corresponding author. E-mail: swebster@creol.ucf.edu.
† CREOL, University of Central Florida.
‡ Georgia Institute of Technology.
§ Institute of Physics, National Academy of Sciences, Ukraine.
⊥ Institute of Organic Chemistry, National Academy of Sciences, Ukraine.
¶ University of Oxford.

10.1021/jp904460f CCC: $40.75
Published on Web 10/20/2009

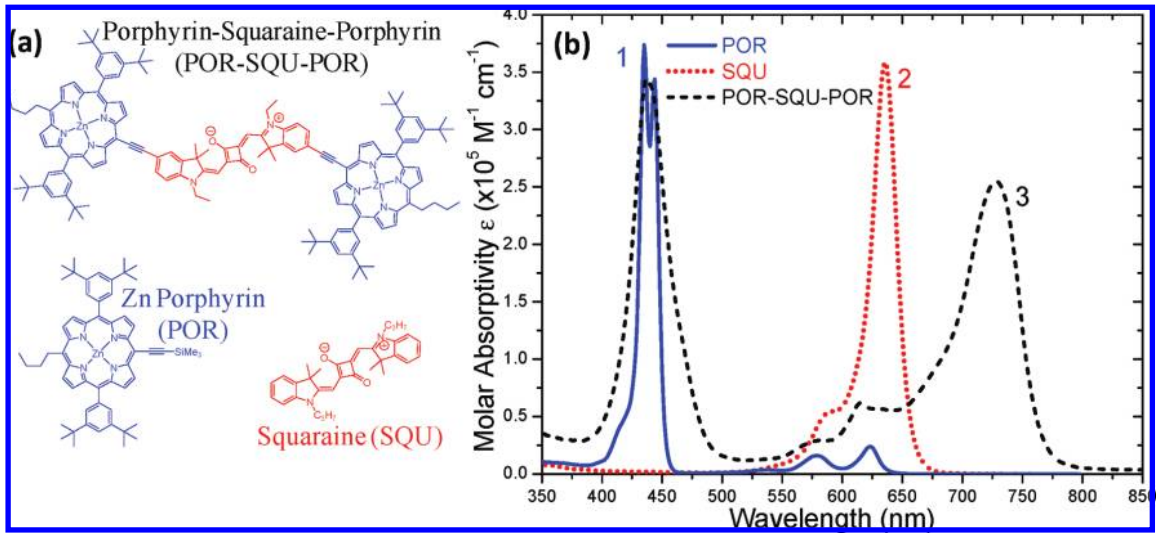

Figure 1. (a) Molecular structures of POR, SQU, and POR-SQU-POR. (b) Molar absorptivities for POR (1), SQU (2), and POR-SQU-POR (3) in DCM + 1% pyridine.

acceptor end groups; (3) overall planarity and rigidity of molecular structures; and (4) symmetry lowering from D_{4h} in the porphyrin monomer to D_{2h} in an array system leading to an increase in the strength of the long wavelength absorbing Q bands.

Linear polymethine-like structures, especially squaraines (which can be regarded as cyanines with a strong acceptor group centered in the vinylene chain), have been shown to exhibit large δ_{2PA} values of up to 35 000 GM[22] owing to their very large ground state transition dipole moments, near-parallel orientation of their ground state transition dipole moments, and the sharply rising low-energy side of their linear absorption that allows significant intermediate-state resonance enhancement of the 2PA[19−24] leading to overall larger cross sections. These molecules are also known for their significant singlet−singlet excited-state absorption (ESA) with peak cross sections of $10^{-16}-10^{-15}$ cm^2, which are comparable to the peak ground-state absorption cross section.[40] The ratio between excited- and ground-state cross sections can be as large as 200 at certain wavelengths.[21−25] However, triplet contributions in the polymethine class of molecules are almost nonexistent with typical singlet excited-state lifetimes of nanoseconds, so that at large fluences, the RSA undergoes a turnover to saturable absorption, reducing their effectiveness for nonlinear transmittance applications.[21,26]

In this study, a porphyrin−squaraine−porphyrin (POR-SQU-POR) molecule consisting of two zinc porphyrin moieties bridged by a squaraine unit has been synthesized and investigated using femto-, pico-, and nanosecond laser pulses with the goal of obtaining a detailed description of the linear and nonlinear optical mechanisms while realizing large and long-lived nonlinear optical responses. Although many derivatives of porphyrins and squaraines with various substituents have been synthesized and studied, to the best of our knowledge, this is the first example of a molecule in which these two classes of compounds are linked together. The molecular linker is an alkyne, the triple bond of which supports planarity and facilitates π-conjugation within the macromolecule. By combining these two moieties into a single "hybrid" conjugated molecule, we have achieved a broadening and increase in δ_{2PA} in the spectral range from 850 to 1600 nm, as recently reported, along with the synthesis of POR-SQU-POR, in a preliminary communication.[27]

Here, we present a more detailed report on the photophysical properties of this compound. We describe the following: (1) linear and two-photon absorption, fluorescence, and excitation and emission anisotropy of POR-SQU-POR and its constituents, a zinc porphyrin (POR) and a symmetrical squaraine (SQU); (2) the experimental methods used for nonlinear absorption measurements including picosecond single pump and double pump−probe,[35] femtosecond two-photon fluorescence, and Z-scans with femto-, pico-, and nanosecond pulsewidths; (3) a detailed analysis of the excited-state decay kinetics and calculation of the singlet−triplet yield; (4) modeling of the molecular excited-state dynamics; and (5) detailed quantum-chemical analysis that provides insight into the nature of the linear and nonlinear optical (NLO) properties. The combination of these experimental methods and theoretical analysis gives us information about the energy-level structure, which agrees with the observed nonlinear absorption processes in POR-SQU-POR.

2. Experimental Methods and Results

2.1. Material Characterization and Linear Spectroscopic Properties. The molecular structures of the dyes studied in this paper are shown in Figure 1a. Derivatives of Zn−porphyrin and squaraine were used as starting materials for the synthesis of the POR-SQU-POR; more details of the synthesis can be found in ref 27. The linear absorption spectra of all molecules, recorded by a Varian Cary 500 spectrophotometer, are presented in Figure 1b with the most significant linear properties listed in Table 1. All measurements were performed in dichloromethane (DCM) containing 1% pyridine, added to improve the chemical stability of POR-SQU-POR, prevent aggregation, and reduce the rate of crystallization, unless otherwise noted. The absorption spectrum of POR in the visible and near UV region is comprised of two bands: a weak intensity Q-band, extending from 500 to 650 nm, and a strong intensity B or Soret band from 400 to 460 nm, which is split into two components due to the asymmetrical structure of the chromophore. The linear absorption spectrum of SQU is composed of an intense cyanine-like band, attributed to the $S_0 \rightarrow S_1$ transition, with a peak at 636 nm and very weak linear absorption in the visible and UV region corresponding to transitions to higher excited-states ($S_0 \rightarrow S_n$). The lowest lying absorption band of POR-SQU-POR, also assigned to $S_0 \rightarrow S_1$, exhibits a red shift of ≈100 nm compared to the corresponding band of the parent squaraine, while the

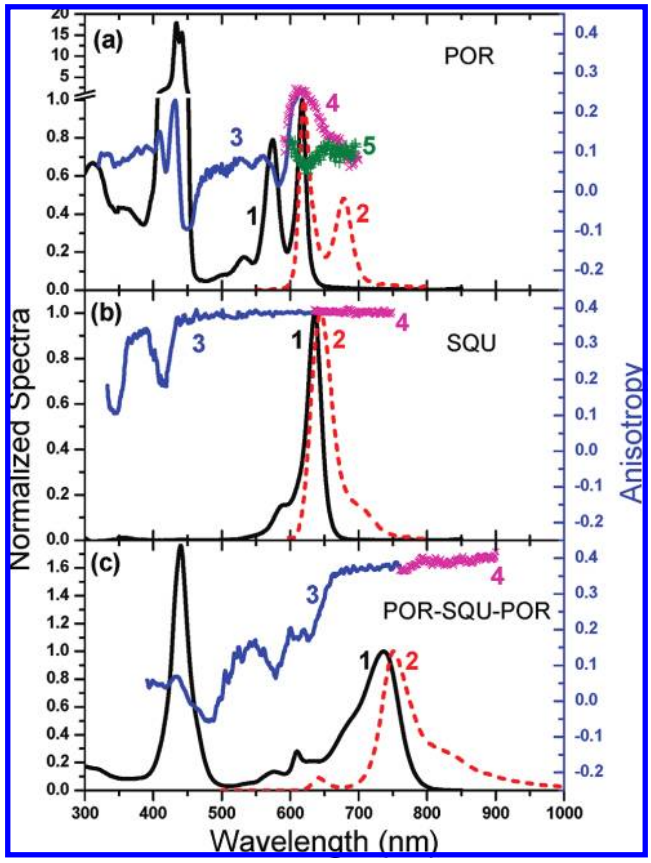

Figure 2. Normalized linear absorption (1), fluorescence (2), excitation anisotropy (3), and emission anisotropy (4 and 5) spectra for POR in pTHF-650 (a), SQU in glycerol (b), and POR-SQU-POR in 1-decanol (c).

next transitions remain nearly unshifted and correspond to the same Q and B bands of the constituent porphyrins. The fluorescence spectra of all compounds, measured by a PTI QuantaMaster spectrofluorimeter equipped with a nitrogen-cooled (77 K) Hamamatsu R5509-73 photomultiplier, are shown in Figure 2. All fluorescence spectra are corrected for the spectral responsivity of the photomultiplier. Fluorescence quantum yields, η, are measured using the standard method of comparison with a known "red" standard dye, Cresyl Violet perchlorate (CAS no. 41830-80-2, Sigma Aldrich) in methanol, which has an absorption peak at 594 nm, fluorescence peak at 620 nm, and a quantum yield, η, of 0.54.[28] Results of the quantum yield measurements are listed in Table 1. From these measurements, we can estimate the fluorescence lifetimes $\tau_F = \eta\tau_R$, where the natural lifetime τ_R can be calculated using the Strickler−Berg equation:[23,29]

$$1/\tau_R = 2.88 \times 10^{-9} n^2 \varepsilon^{max} \left[\frac{\int F(\nu)\, d\nu \int \frac{\varepsilon(\nu)}{\nu}\, d\nu}{\int \frac{F(\nu)}{\nu^3}\, d\nu} \right]$$

where $F(\nu)$and $\varepsilon(\nu)$ are the normalized fluorescence and absorption ($S_0 \rightarrow S_1$) spectral bands, ε^{max} is the extinction coefficient at the peak absorption, and n is the refractive index of the solvent. This equation requires a correct identification of the $S_0 \rightarrow S_1$ absorption band, which is clear for the SQU and POR constituents but is more difficult for POR-SQU-POR due to its strong overlapping of transitions on the higher energy side of the lowest lying absorption band. However, due to a nearly unaltered position of the Q absorption band, the POR contribution can be subtracted for this estimation. Estimated fluorescence lifetimes are the following: 1.2 ± 0.3 ns for POR, 0.7 ± 0.2 ns for SQU, and 0.2 ± 0.04 ns for POR-SQU-POR. These values agree reasonably well with the lifetimes measured by a picosecond pump−probe technique, as discussed in section 2.2.2.

The spectral positions of the optical transitions and the orientation of the transition dipole moments can be determined by one-photon excitation anisotropy measurements. These measurements are performed using a PTI Quantamaster Spectrofluorimeter in viscous solutions to reduce rotational reorientation and at low concentrations ($C \approx 10^{-6}$ M) to avoid reabsorption of the fluorescence. The anisotropy, defined as $r(\lambda) = [I_{||}(\lambda) - I_{\perp}(\lambda)]/[I_{||}(\lambda) + 2I_{\perp}(\lambda)]$, is measured by detecting the emission wavelength, typically near the fluorescence maximum, with a fixed polarization. Then, the fluorescence intensity is recorded as a function of excitation wavelength at polarizations parallel ($I_{||}(\lambda)$) and perpendicular ($I_{\perp}(\lambda)$) to the emission polarization. Detailed information about this technique can be found in ref 30. Our previous studies of anisotropy in cyanine-like dyes, for comparison with the SQU constituent, can be found in refs 19, 20, and 31. Emission anisotropy can be measured and calculated in the same way; the only difference is that these measurements are performed by fixing an excitation wavelength and tuning the emission wavelength through the fluorescence. Emission anisotropy gives information about vibrational molecular depolarization. As shown in Figure 2, excitation anisotropy spectra for all molecules reveal the

TABLE 1: Photophysical Parameters for POR, SQU, and POR-SQU-POR in DCM + 1% Pyridine[a]

	λ^{max}_{Abs}	λ^{max}_{Fl}	ε^{max}	η	τ_F	σ_{01}	σ_{S1n}	σ_{T1n}	τ_F	τ_{ISC}	Φ_T
	nm	nm	10^5 M^{-1} cm^{-1}		10^{-9} sec Estimated from η	10^{-17} cm^2 (532 nm)			10^{-9} sec (532 nm)		
POR	623	626	0.24	0.046 ± 0.005	1.2 ± 0.3	1.3 ± 0.13	5 [5] ± 1	13.5 ± 3	1.9 ± 0.2	7 ± 1.5	0.21± 0.03
SQU	636	642	3.57	0.27 ± 0.03	0.7 ± 0.2	1.28 ± 0.13	15 [20] ± 4		0.9 ± 0.1		
POR-SQU-POR	732	750	2.55	0.06 ± 0.006	0.2 ± 0.04	3.8 ± 0.38	16.5 [15] (15) ± 3	15 ± 3 (8 ± 1.6)	0.21 (0.21) ± 0.05	8 (8) ± 1.6	0.025 (0.025) ± 0.001

[a] The terms λ^{maxAbs} and ε^{max} are the peak absorption wavelength and peak extinction coefficient for the lowest energy transition, $S_0 \rightarrow S_1$; λ^{maxFl} is the peak fluorescence wavelength; σ_{01}, σ_{S1n}, and σ_{T1n} are ground state, singlet−singlet and triplet−triplet excited-state cross sections at 532 nm, respectively; see the model in Figure 5a; η, τ_F, τ_{ISC}, and Φ_T are the fluorescence quantum yield, fluorescence lifetime, intersystem crossing time, and triplet yield, respectively. Note that the nonlinear parameters in red brackets and blue parentheses are determined from fitting picosecond and nanosecond Z-scans, respectively, while the other nonlinear parameters are obtained by fitting picosecond double pump−probe.

alternation of one-photon allowed and symmetry-forbidden transition bands. It is worth noting that this information cannot be obtained from the linear absorption spectra alone. Analysis of the anisotropy spectra, especially when linked to quantum-chemical calculations, can indicate the positions of one-photon forbidden transitions, i.e. transitions between states of the same symmetry, and therefore reveal possible positions of 2PA bands.

Shown in Figure 2a are the absorption, fluorescence, and anisotropy spectra for POR in poly(tetrahydrofuran) of average $M_n \sim 650$ (CAS no. 25190-06-1, Sigma Aldrich, viscosity $\sim$ 100−200 mPas at 30 °C). The absorption peak of the Q-band at 617 nm almost coincides with the fluorescence peak at 620 nm, corresponding to a Stokes shift of ≈3 nm (≈80 cm^{-1}), indicating that the excited-state geometry is not significantly modified from that of the ground state. Additionally, near the main fluorescence band, we observe a weak fluorescence originating from the Soret band with a peak position at ≈450 nm (excitation at 390−430 nm), not shown in Figure 2a. Dual fluorescence bands have previously been reported in porphyrins and originate from the Soret band.[32] Absorption in the Q-band and the corresponding fluorescence show comparatively pronounced vibrational structure related to the skeletal C═C vibrational modes with frequencies of 1200−1300 cm^{-1}. Excitation anisotropy, measured at the emission wavelength fixed near the fluorescence peak (line 3), shows a sharp increase at ≈600 nm overlapping smoothly with the emission anisotropy (line 4). The emission anisotropy spectrum shows a strong depolarization from $r = 0.26$ near the peak position at ≈630 nm to $r = 0.06$ at 690 nm due to vibrational modes. A more detailed analysis of excitation anisotropy for the porphyrin, based on quantum-chemical calculations, is presented in section 3.2.

Figure 2b shows absorption, fluorescence, and anisotropy spectra for SQU in spectrophotometric grade glycerol (CAS no. 56-81-5, Sigma Aldrich, viscosity $\sim$ 900 mPas at 25 °C). The peak absorption and fluorescence were measured at 636 and 644 nm, respectively. As can be seen, the Stokes shift for SQU is slightly larger than that of POR and equals ≈8 nm (195 cm^{-1}) indicating an increased structural flexibility inherent in this molecule. No depolarization is observed within the entire emission range. The excitation anisotropy function $r(\lambda)$ is constant over the broad spectral range from 430 to 600 nm and equals ≈0.4 (line 3), indicating the parallel orientation of the absorption and emission dipole moments within the main absorption band. In the shorter wavelength region, the anisotropy spectrum of SQU shows two features at ≈415 and ≈340 nm corresponding to one-photon forbidden transitions forming 35−45° angles with the emission dipole moment.

Shown in Figure 2c are absorption, fluorescence, and anisotropy spectra for POR-SQU-POR in 1-decanol (CAS no. 112-30-1, Sigma Aldrich, viscosity $\sim$ 11 mPas at 25 °C). The peak absorption and fluorescence were measured at 736 and 756 nm, respectively. As can be seen, the Stokes shift for POR-SQU-POR has increased as compared to SQU and equals ≈20 nm (360 cm^{-1}). In addition to the main fluorescence band, we observe a weak fluorescence originating from the porphyrin component of POR-SQU-POR with a peak position at ≈640 nm (see Figure 2c). The excitation spectrum of this fluorescence band confirms its connection with the POR constituent. The anisotropy spectrum $r(\lambda)$ combines the essential properties of both porphyrin and squaraine parts (line 3): $r(\lambda) \approx 0.4$ in the spectral range from 660 to 760 nm (corresponding to the squaraine part) and follows the main extremes in the porphyrin anisotropy spectrum in the shorter wavelength region. Significant depolarization was not observed within the entire emission range, similar to the behavior of SQU (line 4). More detailed quantum-chemical analysis for this molecule is presented in section 3.4.

2.2. Nonlinear Characterization Methods and Results. Nonlinear optical investigations of POR, SQU, and POR-SQU-POR include a broad range of femto-, pico-, and nanosecond pulsewidth measurements, facilitating a more meticulous study of lifetime dynamics, 2PA, ESA, and singlet−triplet dynamics with self-consistent results across the measured pulsewidths. The femtosecond system is a regeneratively amplified Ti:Sapphire laser (Clark-MXR, model 2010) operating at 1 kHz (∼2 mJ per pulse) at 775 nm, which pumps two optical parametric generator/amplifiers (OPG/OPA Light Conversion Ltd., model TOPAS), providing 100−140 fs pulsewidths (FWHM) measured by 2PA intensity autocorrelation with independently tunable wavelengths from 0.3 to 2.4 μm. The picosecond laser system consists of a 10 Hz modelocked Nd:YAG laser (EKSPLA, model PL2143) with a pulsewidth of 29 ps (FWHM) at 1064 nm which is externally frequency doubled to produce 532 nm with a pulsewidth of 15 ps (FWHM), both measured by second-harmonic autocorrelation. The nanosecond laser system is an externally frequency doubled 10 Hz seeded Nd:YAG laser (Continuum, Powerlight 9010) with a pulsewidth of 3.4 ns (FWHM) measured by a fast silicon detector and digital storage oscilloscope (Tektronix, TDS680C, 1 GHz/5Gs) at 532 nm.

2.2.1. 2PA Spectra. Frequency degenerate 2PA spectra of the sample solutions were measured by two methods: single-wavelength open-aperture Z-scan[33] and two-photon fluorescence (2PF).[34] The Z-scan technique allows for the absolute determination of 2PA cross sections, δ_{2PA}. Focused spot sizes are calibrated at each wavelength by measuring and modeling the nonlinear refraction of a neat solution of carbon disulfide using the closed-aperture Z-scan technique.[35] Detailed descriptions of the Z-scan technique can be found within refs 33 and 35. This method serves as a calibration for focused spot sizes and also as an irradiance calibration to double check the independently measured energy and temporal width of the laser pulse. 2PF was used to measure the 2PA cross sections and calibrated against the well-known 2PA reference, Rhodamine B in methanol,[34] for both POR and SQU. For each wavelength, we checked that the fluorescence signal is quadratically dependent on incident irradiance, indicative of a pure two-photon absorption process. Since the fluorescence spectrum of POR-SQU-POR, red-shifted ≈ 100 nm from the POR and SQU, is beyond the spectral range of our standard 2PF detection system, a NIR optimized photomultiplier tube detector was used to obtain the spectral shape of the 2PA spectrum. This spectrum was then scaled by several open-aperture Z-scan measurements across the spectra to obtain the absolute 2PA cross section. Calibrating results of 2PA Z-scan measurements are shown in Figure 3 as solid data points. At 860 nm, POR was measured by both the open-aperture Z-scan and the 2PF technique, both showing excellent agreement in absolute magnitude.

Experimental one-photon and degenerate 2PA spectra for POR, SQU, and POR-SQU-POR are presented in Figure 3 with the 2PA spectrum plotted on a semilogarithmic scale. For comparison of transition wavelength, all spectra are shown on the same graph with separate axes for linear one-photon absorption (bottom) and 2PA (top) photon wavelengths. As shown, POR is characterized by two weak 2PA bands. The first 2PA band with $\delta_{2PA} \approx 10$ GM corresponds to two-photon excitation into the Q-band. We observed an increase of δ_{2PA} to 50 GM at shorter excitation wavelengths; however, the peak of the second band cannot be fully resolved due to the tail of the

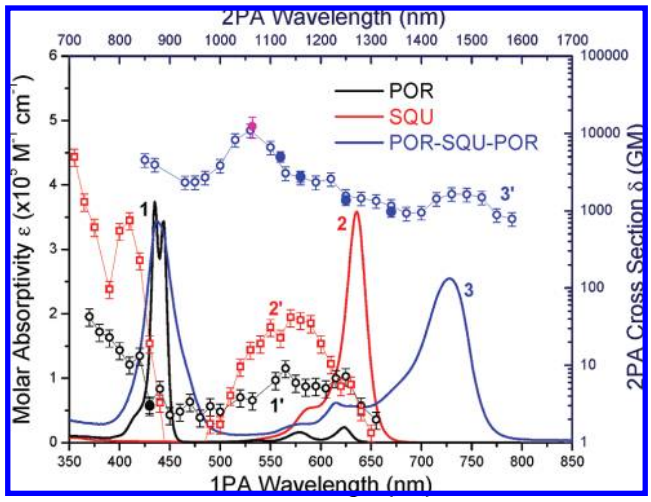

Figure 3. Molar absorptivity and 2PA spectra for POR (1,1′), SQU (2,2′), and POR-SQU-POR (3,3′) in DCM + 1% pyridine. Open and closed 2PA data were obtained by 2PF and open-aperture Z-scan, respectively. The solid pink data point at 1064 nm was obtained by picosecond open-aperture Z-scan for POR-SQU-POR.

linear absorption of POR. The 2PA cross section for SQU is much larger. The nature of the 2PA bands for SQU and similar dyes have been investigated previously.[20,23,31] As seen from Figure 3, the experimentally observed 2PA spectrum includes 4 bands: a relatively weak band with $\delta_{2PA} \approx 40$ GM corresponding to the 2PA excitation into the vibronic shoulder of the strongly one-photon-allowed $S_0 \rightarrow S_1$ transition, the first two-photon allowed transition (assigned to $S_0 \rightarrow S_2$) at 1100 nm, a more intense band with $\delta_{2PA} \approx 750$ GM (two-photon excitation at 820 nm), and a high intensity band with δ_{2PA} up to at least 5200 GM (two-photon excitation at 710 nm). The peak of the fourth band is also not resolved due to the tail of the linear absorption. The 2PA spectrum for the POR-SQU-POR, by contrast, is very broad and covers the entire measurable region with δ_{2PA} ranging from 780 GM (two-photon excitation at 1580 nm) up to 11 000 GM (two-photon excitation at 1060 nm). A detailed analysis based on quantum-chemical calculations is presented in section 3.

2.2.2. Decay Kinetics. In order to understand and model the nonlinear absorption processes, the fluorescence lifetimes and population dynamics must be understood. Estimation of fluorescence lifetimes performed from the steady-state measurements indicate that the investigated compounds are characterized by lifetimes ranging from 200 ps to 1.2 ns; hence, the use of a picosecond laser system is appropriate for these measurements. In pump−probe measurements, a strong linearly polarized pump pulse excites the molecules and creates a population distribution in the excited-state which can be monitored as a function of time by a less intense probe pulse. In our experiments, both pump and probe beams at 532 nm were focused to spot sizes of ≈70 and ≈35 μm (HW1/e^2), respectively. The probe beam can be delayed up to 15 ns, and its fluence was kept much smaller than that of the pump (probe approximately 0.1% of the pump fluence) to avoid probe nonlinearities. Pump and probe beams were overlapped at a small angle ≈5° within the sample and with the probe beam polarized at the "magic" angle (54.7°) with respect to the pump in order to avoid contributions from reorientation effects. Under these conditions, the probe decay is completely independent of polarization anisotropy, monoexponential, and corresponds to the lifetime τ_F.[30,36] In order to determine the triplet yield Φ_T, i.e., the percentage of the population moved from the singlet to triplet state, and to calculate the intersystem crossing lifetime τ_{ISC}, i.e., how quickly population is moved from the singlet to triplet state, we utilize a picosecond double pump−probe technique which has been shown to determine both singlet and triplet lifetimes and cross sections.[37] The setup consists of the standard pump−probe described above but has been modified to include a second pump at a fixed delay of ≈6 ns. In general, to fully determine the singlet−triplet dynamics, both picosecond single pump−probe and nanosecond Z-scan must be performed in order to decouple the triplet intersystem crossing rate and yield. The double pump−probe technique allows the determination of singlet−triplet dynamics in one measurement, greatly reducing the measurement error inherent in the use of multiple techniques across an order of magnitude in pulsewidths.

ESA in the form of RSA and triplet−triplet absorption is best described by a five-level model shown schematically in Figure 5a. The propagation and rate equations are described by (1):

$$
\begin{aligned}
\frac{dI}{dz} &= -\sigma_{01}N_0 I - \sigma_{S1n}N_{S1} I - \sigma_{T1n}N_{T1} I \\
\frac{dN_0}{dt} &= -\frac{\sigma_{01}N_0 I}{\hbar\omega} + \frac{N_{S1}}{\tau_F} + \frac{N_{T1}}{\tau_{phos}} \\
\frac{dN_{S1}}{dt} &= \frac{\sigma_{01}N_0 I}{\hbar\omega} - \frac{N_{S1}}{\tau_F} - \frac{\sigma_{S1n}N_{S1} I}{\hbar\omega} + \frac{N_{Sn}}{\tau_{Sn1}} - \frac{N_{S1}}{\tau_{ISC}} \\
\frac{dN_{Sn}}{dt} &= \frac{\sigma_{S1n}N_{S1} I}{\hbar\omega} - \frac{N_{Sn}}{\tau_{Sn1}} \\
\frac{dN_{T1}}{dt} &= -\frac{\sigma_{T1n}N_{T1} I}{\hbar\omega} + \frac{N_{Tn}}{\tau_{Tn1}} + \frac{N_{S1}}{\tau_{ISC}} - \frac{N_{T1}}{\tau_{phos}} \\
\frac{dN_{Tn}}{dt} &= \frac{\sigma_{T1n}N_{T1} I}{\hbar\omega} - \frac{N_{Tn}}{\tau_{Tn1}}
\end{aligned}
\tag{1}
$$

where N_0, N_{S1}, N_{Sn}, N_{T1}, and N_{Tn} are the populations of each level ($N_{total} = N_{S0} + N_{S1} + N_{Sn} + N_{T1} + N_{Tn}$); σ_{01}, σ_{S1n}, and σ_{T1n} are the absorption cross sections from the ground, first singlet excited, and the lowest triplet excited-states, respectively. Modeling for the picosecond pump−probe measurements assumes that the upper excited singlet, S_n, and triplet, T_n, states are not significantly populated; therefore, corresponding lifetimes τ_{Sn} and τ_{Tn} can be neglected, an assumption which has been verified by picosecond Z-scan (see section 2.2.3). The triplet yield Φ_T is determined from $\Phi_T = \tau_F/(\tau_F + \tau_{ISC})$. All of the modeling in this paper assumes that the recovery from the triplet to the ground singlet state is slow and can be neglected, i.e., that the phosphorescence lifetime τ_{phos}, is much longer than tens of nanoseconds. The remaining fitting parameters are the singlet−singlet and triplet−triplet excited-state cross sections and the fluorescence and intersystem crossing lifetimes, of which the fluorescence lifetime and the singlet−singlet excited-state cross sections may be cross-checked by the fluorescence quantum yield measurements and picosecond Z-scan, respectively.

Frequency degenerate pump−probe results at 532 nm for POR, SQU, and POR-SQU-POR are presented in Figure 4. As can be seen in Figure 4b, the SQU dye shows a complete transmittance recovery during ≈6 ns, confirming that triplet states are not measurably populated, $\Phi_T \approx 0$, and can be neglected for nonlinear absorption modeling of this dye in the femto-, pico-, and nanosecond time regimes. However, for POR, as shown in Figure 4a, the decay kinetics are biexponential and include both singlet and triplet states, recovering with a triplet yield and intersystem crossing lifetime of $\Phi_T \approx 0.21$ and τ_{ISC}

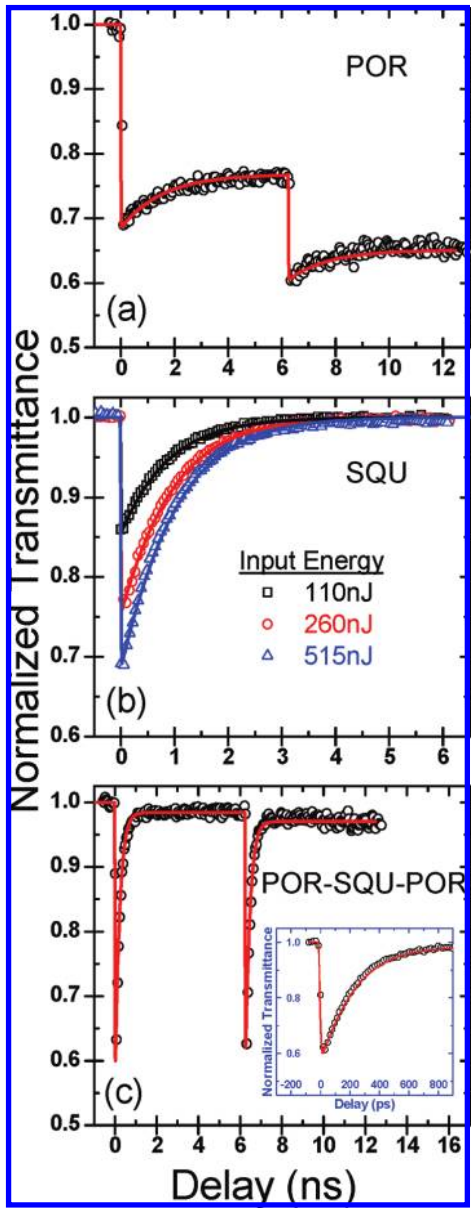

Figure 4. Picosecond pump−probe results at 532 nm for POR (a), SQU (b), and POR-SQU-POR (c) in DCM + 1% pyridine. The inset shows short delay scan of POR-SQU-POR.

≈ 7 ns. For POR-SQU-POR, shown in Figure 4c, the contribution of the triplet state is much smaller than for the porphyrin itself but is still measurable: $\Phi_T \approx 0.025$ and $\tau_{ISC} \approx 8$ ns. The recovery of the population to the ground state for POR-SQU-POR is also much faster than that of the individual molecules, inset of Figure 4c. In general this can be understood from the ≈100 nm red shift of the main absorption band, which typically leads to a significant decrease of the fluorescence quantum yield due to a decrease in energy gap between the ground and first excited-state and, thus, a reduced excited-state lifetime. The fluorescence lifetimes obtained from picosecond single and double pump−probe are the following: 1.9 ± 0.2, 0.9 ± 0.1, and 0.21 ± 0.05 ns in reasonable agreement with the estimated values obtained from the absorption and fluorescence spectra and quantum yield 1.2 ± 0.3, 0.7 ± 0.2, and 0.2 ± 0.04 ns for POR, SQU, and POR-SQU-POR, respectively.

2.2.3. Pico- and Nanosecond Z-Scan Measurements: RSA and 2PA-Induced ESA. RSA for POR-SQU-POR was measured by picosecond and nanosecond Z-scans at 532 nm and is shown in Figures 5b and c, respectively. Both results were modeled with the propagation and rate eqs. 1 and correspond to the energy-level schematic in Figure 5a. In order to fully characterize the RSA properties of POR-SQU-POR, the measurements where performed with input energies spanning 2 orders of magnitude. The picosecond Z-scan results were modeled by a simplified 3-level system, including only singlet states since the triplet state is not significantly populated during the 15 ps pulsewidth. Using the already determined excited-state lifetime τ_F, the picosecond Z-scans and their fitting allow the determination of the singlet excited-state cross section, $\sigma_{S1n} \approx 15 \times 10^{-17}$ cm^2, shown in Table 1 (red brackets), which was found to be in excellent agreement with the picosecond double pump−probe measurement of $\sigma_{S1n} \approx 16.5 \times 10^{-17}$ cm^2. The upper excited-state lifetime, $\tau_{Sn1} \sim 200$ fs, validates our assumption that the population of the upper singlet excited-state can be neglected in modeling the pump−probe data but was not neglected in the Z-scan analysis due to the large input energies. Note that for the largest energy measured (563 nJ in Figure 5b), the modeling and Z-scan results indicate that the first excited-state has become significantly populated and the RSA changes to saturable absorption and the characteristic "turnover" has been reached. Excited-state cross sections and upper excited-state lifetimes for POR and SQU were also determined from additional picosecond Z-scans (data not shown) to be ≈5 × 10^{-17} cm^2 and ≈500 fs for POR and ≈20 × 10^{-17} cm^2 and ≈3 ps for SQU, which also agree (within ∼25%) with the pump−probe measurements.

Nanosecond Z-scan results at 532 nm for POR-SQU-POR, presented in Figure 5c, were fit using the five-level model (eq

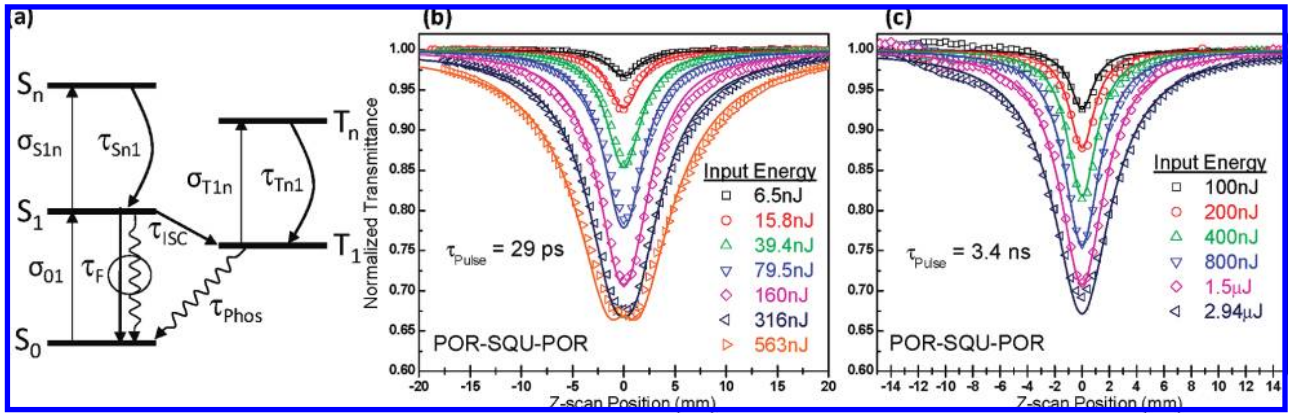

Figure 5. (a) Five-level energy schematic including singlet and triplet excited-state absorption. Modeled (solid curves) and experimental picosecond (b) and nanosecond (c) open-aperture Z-scan data at 532 nm in DCM + 1% pyridine.

1) including both singlet and triplet states; τ_F and σ_{S1n} were determined from picosecond pump−probe and Z-scan measurements. The results are shown in Table 1 (data in blue parentheses). The triplet yield $\Phi_T \approx 0.025$ was found to be in excellent agreement with the picosecond double pump−probe ($\Phi_T \approx 0.025$), and therefore, the intersystem crossing lifetime too. However, the triplet cross section σ_{T1n} was determined to be $\approx 8 \times 10^{-17}$ cm^2, which is roughly half of the value obtained by picosecond double pump−probe. The reason for this discrepancy is unknown, but we speculate that this may be due to an increased photochemical instability with longer nanosecond pulsewidths and larger input fluences. These parameters were determined to be the best-fit to the data for input energies ranging from 100 nJ to almost 3 μJ.

To determine the 2PA-induced ESA, picosecond Z-scan measurements were performed at 1064 nm for POR-SQU-POR. These results are presented in Figure 6. Shown in Figure 6a is a five-level energy schematic consisting of all singlet states used in modeling the experimental data in Figure 6b. The propagation and rate equations for 2PA-induced ESA are described as follows:

$$\begin{aligned}
\frac{dI}{dz} &= -\frac{\delta_{2PA}N_0I^2}{\hbar\omega} - \sigma_{1n}N_1I - \sigma_{1'm}N_{1'}I \\
\frac{dN_0}{dt} &= -\frac{\delta_{2PA}N_0I^2}{2(\hbar\omega)^2} + \frac{N_1}{\tau_F} + \frac{N_{1'}}{\tau_{1'0}} \\
\frac{dN_1}{dt} &= \frac{\delta_{2PA}N_0I^2}{2(\hbar\omega)^2} - \frac{N_1}{\tau_F} - \frac{\sigma_{1n}N_1I}{\hbar\omega} + \frac{N_{1'}}{\tau_{1'1}} \\
\frac{dN_{1'}}{dt} &= -\frac{\sigma_{1'm}N_{1'}I}{\hbar\omega} + \frac{N_m}{\tau_{m1'}} + \frac{N_n}{\tau_{n1'}} - \frac{N_{1'}}{\tau_{1'1}} - \frac{N_{1'}}{\tau_{1'0}} \\
\frac{dN_n}{dt} &= \frac{\sigma_{1n}N_1I}{\hbar\omega} - \frac{N_n}{\tau_{n1'}} \\
\frac{dN_m}{dt} &= \frac{\sigma_{1'm}N_{1'}I}{\hbar\omega} - \frac{N_m}{\tau_{m1'}}
\end{aligned} \tag{2}$$

where N_0, N_1, $N_{1'}$, N_n, and N_m are the populations of each level ($N_{total} = N_0 + N_1 + N_{1'} + N_n + N_m$); δ_{2PA}, σ_{1n}, and $\sigma_{1'm}$ are the two-photon, first excited, and upper excited-state absorption cross sections, respectively. The fluorescence lifetime, τ_F, was determined from picosecond pump−probe at 532 nm. The higher energy fluorescence lifetime, $\tau_{1'0}$, which we associate with the fluorescence band at ~640 nm in Figure 2c, has an estimated natural lifetime of ~10 ns and quantum yield of ~0.2%, which is therefore neglected in the rate equations. The highest excited-states S_n and S_m in the modeling were assumed not to be populated since the lifetimes $\tau_{n1'}$ and $\tau_{m1'}$ are ultrafast (shorter than 500 fs) and, therefore, can also be neglected, simplifying the rate equations in eq 2. Although not obvious in Figure 6b, the analysis of the nonlinear response for POR-SQU-POR at 1064 nm with picosecond pulsewidths is complicated. Shown in Figure 6c is a helpful way of organizing Z-scan results to extract contributions from various nonlinear absorption mechanisms. The Z-scan data is processed by only considering the minimum transmittance at focus for each energy and then independently fitting each value with a pure 2PA model, regardless of what additional nonlinear absorption mechanisms are present in the sample, and hence is referred to as an *effective* 2PA. This method can be useful in developing a realistic model, but disregards the additional information contained in the Z-scan curves. Once a realistic model is constructed, the full propagation and rate equations must be used to determine one set of parameters to fit all of the Z-scan curves, as was done in Figure 6b. Pure 2PA, or effective 2PA, is modeled by[35]

$$T(z, S = 1) = \frac{-1}{\sqrt{\pi}q_o(z,0)} \int_{-\infty}^{\infty} \ln[1 + q_o(z,0)e^{-t^2}]\, dt \tag{3}$$

where $q_o(z,t) = \beta I_o(t)L/(1 + z^2/Zo^2)$, L is the sample length, Zo is the Rayleigh range, $I_o(t)$ is the irradiance, and z is the sample position. The effective 2PA coefficient, β_{eff}, which has been converted to an effective 2PA cross section for clarity, is plotted verses the input peak irradiance as is shown in Figure 6c, labeled as data 1. For the simplest pure 2PA process, including no saturation, the cross section is constant with respect to irradiance (shown in Figure 6c, line 2). However, if there are additional nonlinear mechanisms, i.e. ESA without saturation, the effective 2PA cross section will increase above line 2 with increasing irradiance. A simple way to estimate the pure 2PA is to linearly

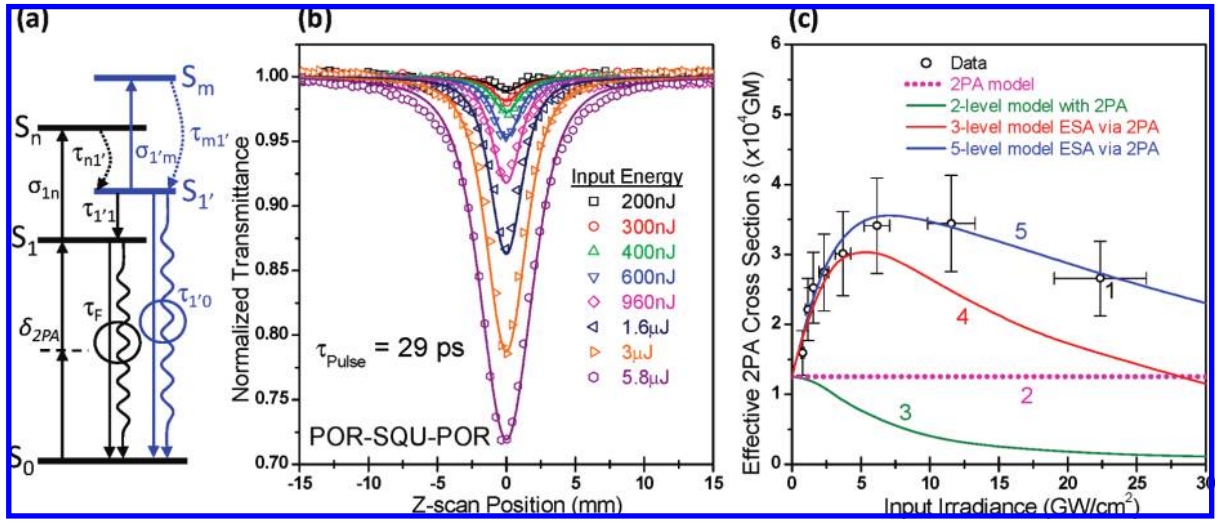

Figure 6. (a) Five-level energy schematic of singlet excited-state absorption via 2PA. (b) Modeled (solid curves) and experimental picosecond open-aperture Z-scan data at 1064 nm in DCM + 1% pyridine. (c) Effective 2PA cross section verses input peak irradiance. Experimental data (1, black open circles with error bars) are modeled with pure 2PA (2), a two-level model with 2PA (3), three-level ESA with 2PA (4), and a five-level model (5).

extract the slope of the first few data points and use the *y*-intercept value as the pure 2PA cross section. One obvious difficulty is how to ensure that the first few energies that have been measured can be used to accurately extract a meaningful 2PA cross section. If the first two energies could not have been measured, due to insufficient detector signal-to-noise or other difficulties, this method would have led to a value of ~22 000 GM, nearly twice that expected. This method therefore can only be used for order-of-magnitude measurements, but more detailed modeling is needed to extract meaningful data, especially when reporting large 2PA cross sections. An additional feature can be observed when plotting the data in this form. At larger input irradiances, a decrease in 2PA cross section is experimentally observed. This behavior is explained by saturation of 2PA at our concentration of 0.7 mM. If a significant number of molecules are moved into an excited-state with a lifetime longer than the pulsewidth, the ground-state population becomes depleted, resulting in saturation of the 2PA. Although not normally considered, saturation of 2PA has been reported by several research groups[38,39] and must be considered under our experimental conditions. Another possibility is chemical degradation induced by either photochemical or thermal instabilities. To control the contribution of degradation, this sample was measured within a few hours of preparing the solution and by carefully checking the linear absorption spectra before and after measurements. These results allow us to exclude the influence of sample degradation from our analysis.

The simulated line 3 in Figure 6c is based on a two-level model (S_0 and S_1 from Figure 6a) using 2PA excitation with a pulsewidth of 29 ps (FWHM) at 1064 nm, which is much shorter than $\tau_F \approx 210$ ps. Clearly, the 2PA easily becomes saturated. Line 4 in Figure 6c is simulated with an effective 3-level model, using our sample parameters and femtosecond measured 2PA at 1064 nm, using a best fit approach. A satisfactory 2PA value is obtained, by appropriate weighting of the first few irradiance points, but at input irradiances larger than 5 GW/cm^2, the increased nonlinear absorption from one ESA level is not large enough to counter the 2PA saturation and additional absorption is needed to explain the data. To correctly explain all the data at 1064 nm, a full five-level model (Figure 6a, line 5) is considered, which is simplified by assuming no population in the highest excited-states S_n and S_m. With these assumptions, and the knowledge of the previously mentioned parameters, the model is reduced to only two unknowns, σ_{1n} and $\sigma_{1'm}$, with eight fitting energies spanning several orders of magnitude, with verification of, or cross-check, of 2PA (from femtosecond), τ_F (from picosecond pump−probe and additionally estimated from quantum yield and absorption/fluorescence spectra), $\tau_{1'0}$ (from estimated η and absorption/fluorescence spectra), and N_{total} (from molar absorptivity). The five-level model, presented in Figure 6a, is based on data obtained from linear spectroscopy results (section 2.1) and quantum-chemical calculations (section 3.4) supporting the idea that electronic transitions in POR-SQU-POR can be separated into three groups: electronic transitions within the POR fragments; transitions within the SQU; and POR to SQU charge-transfer transitions. The 2PA at 1064 nm populates the first excited-state, S_1, which is connected with a charge distribution primarily within the SQU fragment. Excited-state absorption from this level at 1064 nm (with cross section σ_{1n}) corresponds to the population of the Soret band in the POR part of the POR-SQU-POR (S_n level) followed by an ultrafast transition (with $\tau_{n1'}$) into the lower POR Q-band ($S_{1'}$ level). Additional excited-state absorption from this level with cross section $\sigma_{1'm}$ (and ultrafast depopulation of the S_m state with $\tau_{m1'}$) increases the nonlinear absorption and counters the observed 2PA saturation. A lifetime $\tau_{1'1} \approx 1$ ps was determined from the model and found to be in agreement with the estimated value from the observed fluorescence of the POR fragment in POR-SQU-POR (see Figure 2c and explanation in section 2.1). After this intensive analysis, the 2PA cross section was calculated to be 12 400 ± 2500 GM and is found to be in excellent agreement with the femtosecond 2PF measurements at 1064 nm. The 2PA induced ESA at 1064 nm from S_1 and $S_{1'}$ levels were determined to be $\sigma_{1n} \approx 1 \times 10^{-17}$ cm^2 and $\sigma_{1'm} \approx 1.5 \times 10^{-17}$ cm^2.

3. Quantum-Chemical Analysis and Discussion

3.1. Quantum-Chemical Approach. Quantum-chemical orbital analysis is performed with the goal of understanding the following: (1) the linear absorption spectra of POR-SQU-POR, (2) changes in the singlet−triplet dynamics, and (3) the nature of increased 2PA for POR-SQU-POR in comparison with the spectra of individual POR and SQU molecules. All calculations are performed for slightly simplified molecular structures, neglecting the *tert*-butyls, *n*-butyl, and alkynyl bridge in the POR unit. *tert*-Butyl and *n*-butyl are excluded from the calculations since the weak inductive effects anticipated from these substituents are not expected to affect the main spectroscopic characteristics. The alkynyl bridging group is also neglected since comparison of the spectra of the alkynylated model compound and zinc tetraphenylporphyrin suggests that these substituents have only minor effects on the spectroscopic characteristics. Optimal geometries for the POR, SQU, and POR-SQU-POR molecules were calculated with the ZINDO1 method from the HyperChem package. The procedure of geometry optimization was stopped when the energy gradient reached 0.01 kcal/mol. It is worth noting that the AM1 method, often applied for the geometry optimization of linear conjugated molecules, gives a slightly asymmetrical bond-length distribution for the POR, which is probably connected with the incorporation of Zn into the porphyrin. However, the symmetry of the molecular geometry is conserved with the use of the ZINDO1 method. POR-SQU-POR exhibits similar bond lengths within its POR and SQU constituent parts to those in the separate POR and SQU molecules. The length of the SQU including the alkynyl bridges is ~29Å, while the total length of the POR-SQU-POR is ~39Å. The methodology for the calculation of the positions of the electronic levels and shapes of their molecular orbitals (MOs) is described in refs 19, 20, and 40. This is a useful tool for understanding the nature of the orbitals and the transitions between them, including calculation of peak positions of 2PA and ESA. It has been applied previously to obtain a detailed understanding of the linear and nonlinear absorption properties in a series of polymethine, squaraine, and tetraone dyes.[40] The energies of the MOs, electronic transitions between them, and oscillator strengths were calculated in the framework of the standard semiempirical ZINDO/SCI method.[41] In our calculations, we considered only a single-excitation configuration interaction scheme (SCI), since our goal was to reproduce the linear absorption spectra of all investigated molecules. With the linear absorption calculated, a symmetry analysis was performed to predict possible 2PA transitions by identifying one-photon allowed and forbidden transitions. It should be noted that for some organic chromophores, higher-order configuration−interaction schemes may give more accurate results for 2PA energies and cross sections. However for cyanine-like molecules, our previous observations and theoretical predictions for a variety of linear and nonlinear optical properties are in good agreement and have provided us with confidence that a SCI approach can be used. For the POR-

SQU-POR molecule, the modeling is more complex due to the larger size of the molecule. Therefore, while a more extensive CI space may produce a more accurate description of 2PA spectra of extended porphyrin-containing molecules, this is computationally expensive and, in conjunction with the extensive experimental data we have obtained, valuable insights may be gained by use of the ZINDO-SCI methodology.

The wave function of the ith MO φ_i was written as an expansion of the atomic orbitals χ_μ: $\varphi_i = \sum_\mu C_{i\mu}\chi_\mu$, where the $C_{i\mu}$ are the corresponding coefficients and the summation runs over all atomic orbitals. The shape of the MOs is defined by the coefficients $C_{i\mu}$ allowing analysis of the symmetry of the wave functions φ_i. We note that $C_{i\mu}^2$ represents the probability of the location of an electron in the ith MO in the neighborhood of the μth atom or charge density distribution as described in refs 19, 20, and 40. The wave functions of the excited-states were built with the SCI technique taking into account 3 occupied and 3 unoccupied MOs for POR (a total of 9 configurations), 5 occupied and 4 unoccupied MOs for SQU (a total of 20 configurations), and 6 occupied and 6 unoccupied MOs for the macromolecule POR-SQU-POR (a total of 36 configurations). We have verified that this number of configurations is sufficient to model the one- and two-photon absorption properties of the molecules studied in the near UV, visible, and NIR ranges that are covered by the experimentally measured spectra as described in more detail in sections 3.2−3.4. In all cases, the ordering of these MOs was checked by an ab initio method (6-31G** basis).

3.2. Quantum-Chemical Calculations for the POR Molecule. Figure 7 represents the scheme of the highest occupied MO (HOMO), two occupied MOs below the HOMO (HOMO − 1 and HOMO − 2), the lowest unoccupied MO (LUMO), two unoccupied MOs above the LUMO (LUMO + 1 and LUMO + 2), the shapes of MOs, and corresponding transitions between them for the zinc porphyrin molecule. The main spectroscopic properties of many porphyrin molecules can be explained by the four-orbital Gouterman model taking into account only four MOs: HOMO, HOMO − 1, LUMO, and LUMO + 1.[1,2] The LUMO and LUMO + 1, which are almost degenerate, are well-separated from the next LUMO + 2 level with an energy gap of ≈1.2 eV. A similar separation is observed between HOMO − 1 and HOMO − 2, while HOMO and HOMO − 1 levels are placed much closer (≈0.8 eV) confirming the reliability of the four-orbital model. The standard interpretation of their linear absorption spectra in the visible and near UV region is the following. The nature of the Q-band, which absorbs from 500 to 630 nm, is mainly related to transitions from the HOMO to degenerate LUMO and LUMO + 1, and the nature of the B or Soret band, which ranges from 400 to 460 nm, is mainly related to transitions from the HOMO − 1 to the same degenerate LUMO and LUMO + 1.

The positions of the singlet (E_S) and triplet (E_T) states have previously been calculated using the following: $E_S = E_i - E_j + 2K_{ij} - J_{ij}$ and $E_T = E_i - E_j - J_{ij}$, where E_i and E_j are the energies of i and j molecular orbitals; K_{ij} is the resonance integral connected with the overlapping of the wave functions between the corresponding orbitals; J_{ij} is a Coulomb integral connected with the interaction of the electrons in the molecule.[42] From these relations, the singlet−triplet splitting energy, ΔE_{ST}, depends on the resonance integral K_{ij} between the corresponding orbitals. For the POR molecule, the splitting energy between the lowest singlet and triplet states is relatively small, $\Delta E_{ST} \approx$ 0.4−0.5 eV,[43] which is in agreement with the small overlapping of HOMO with degenerate LUMO and LUMO + 1 (quasi-forbidden transitions). This small singlet−triplet splitting increases the intersystem crossing rate, which was measured experimentally and is presented in section 2.2.2.

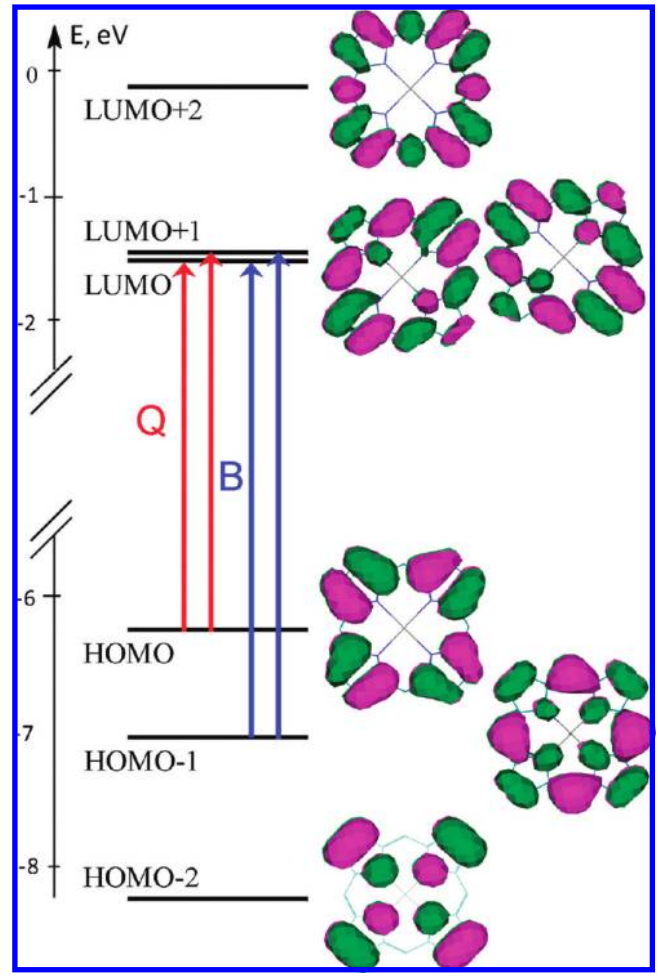

Figure 7. Schematic of molecular orbital energy-levels with corresponding transitions, within a one electron approximation, and charge density distribution for POR.

Quantum-chemical calculations allow us to understand the results of the steady-state excitation and emission anisotropy for the POR molecule presented in Figure 2a. (1) The excitation anisotropy spectrum measured at the fixed wavelength of 630 nm, close to the emission peak (curve 3), shows alternation of two singlet states (doublets) within each Q (615−620 and 520−530 nm) and B (420−430 and 440−450 nm) band. (2) Transitions corresponding to 620 and 450 nm (doublets due to splitting of the HOMO → LUMO and HOMO → LUMO + 1), as well as transitions corresponding to 520 and 420 nm (doublets due to splitting of the HOMO − 1 → LUMO and HOMO − 1 → LUMO + 1), have the same nature but nearly opposite orientation of their dipole moments, as illustrated by the anisotropy curve 3 in Figure 2a. (3) The emission anisotropy spectrum (curve 4, excitation at 430 nm) shows a strong depolarization from $r = 0.26$ near the peak position ≈630 nm to $r = 0.06$ at 690 nm due to vibrations. (4) Only emission fixed at the peak of 630 nm can show alternation of the absorption dipoles in the excitation anisotropy spectrum. (5) Only excitation at 430 and 615 nm can show the peak in emission anisotropy due to a nearly parallel orientation of their excitation and emission dipole moments. An opposite trend (however, much less pronounced) with anisotropy minima corresponding to the former peaks is observed at excitations of 450 and 570 nm (curve 5), corresponding to a large angle

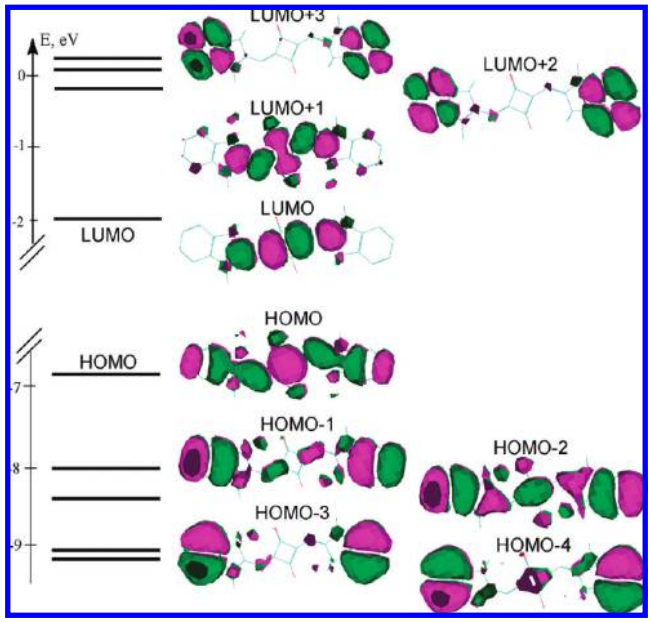

Figure 8. Schematic of molecular orbital energy levels and charge density distribution for SQU.

between the excitation and emission dipole moments. (6) The excitation anisotropy spectrum at 690 nm (curve 3) indicates that $r \approx 0.1$ for a broad wavelength range. This effect can be observed if the transition dipole moments are randomized (presumably by vibrations) due to the highly symmetrical POR molecule. A similar case was described for a triphenylene molecule by Lakowicz; see ref 26 for more details.

3.3. Quantum-Chemical Calculations for the SQU Molecule. Figure 8 shows the energy-level diagram and charge density distributions for the SQU molecule. The electronic structure of the SQU molecule is characterized by the insertion of the acceptor C_4O_2 fragment at the center of the conjugated polymethine chain, making this molecule overall neutral. The SQU molecule belongs to the C_i symmetry group with an inversion center. In our ZINDO/SCI calculations, the number of the molecular orbitals was limited to nine: from HOMO to HOMO − 4 and from LUMO to LUMO + 3, allowing an understanding of the main spectroscopic properties of the SQU, in agreement with our previous papers.[20,40] In this case, quantum-chemical orbital analysis allows a distinction between several types of molecular orbitals: two donor-occupied orbitals, HOMO and HOMO − 1, originating from the donor nitrogen atoms and extending to the chain; local-occupied HOMO − 3 and HOMO − 4, originating primarily from the benzene rings of the terminal groups; and delocalized HOMO − 2 and LUMO + 1 spreading out over the entire molecule. The LUMO + 2 and LUMO + 3 can be attributed to the local orbitals of the terminal groups with charge distribution located primarily on the benzene rings. The LUMO level is characterized by charge distribution within the vinylene chain only. Note that symmetrical and asymmetrical pairs of donor (HOMO and HOMO − 1) and local orbitals (HOMO − 3 and HOMO − 4; LUMO + 2 and LUMO+3) are formed from the doubly degenerate orbitals as a result of their splitting, leading to charge redistribution. Therefore, the corresponding transitions are characterized by very different oscillator strengths.

The first intense allowed $S_0 \rightarrow S_1$ transition for SQU, being of $1A_g \rightarrow 1B_u$ symmetry, is connected with electron transfer from HOMO to LUMO. Due to the very large overlap integral K_{ij} between HOMO and LUMO, the singlet−triplet splitting energy is extremely large: $\Delta E_{ST} \approx 1.7-1.8$ eV, leading to a very low energy position of the first triplet state. Therefore, the intersystem crossing rate for the SQU molecule is expected to be extremely small, and the population of the triplet state is expected to be negligible, which is typical for most cyanine-like molecules as is confirmed experimentally. The next $S_0 \rightarrow S_2$ transition primarily involves the asymmetrical donor HOMO − 1 and asymmetrical LUMO. This transition, being of $1A_g \rightarrow 2A_g$ symmetry, is characterized by a much smaller oscillator strength; it is covered by the shoulder of the $S_0 \rightarrow S_1$ band and, therefore, cannot be resolved in the excitation anisotropy spectrum. The anisotropy minima at ~415 and ~340 nm suggest the positions of one-photon forbidden transitions $1A_g \rightarrow 4A_g$ and $1A_g \rightarrow 6A_g$.

3.4. Quantum-Chemical Calculations for POR-SQU-POR. In order to estimate the number of configurations sufficient to model the one- and two-photon absorption properties in POR-SQU-POR and understand the formation of energy-levels in this molecule, we first performed the calculations for a POR dimer, in which two POR molecules are connected by a conjugated oligo(phenylenevinylene) chain with a length ≈29 Å, which corresponds to the length of the SQU bridge in POR-SQU-POR. As mentioned previously, for a molecule of this size and complexity, the SCI approach may be inadequate to describe the true electronic structure, but insights into the evolution of the electronic structure of the constituent parts of the POR-SQU-POR to the entire molecule are possible. With this caveat, Figure 9 shows the evolution of the MOs and charge density distributions from the Zn-POR molecule to POR dimer. For the description of the POR dimer, it is necessary to involve a larger numbers of MOs than for POR itself. Instead of two degenerate states, LUMO and LUMO + 1, as was the case for the POR molecule, there are two pairs of degenerate unoccupied MOs, separated by a small energy of ≈0.1 eV. These four orbitals are characterized by charge localization at the POR parts only. Note that the splitting energy between LUMO and LUMO + 1, as well as between LUMO + 2 and LUMO + 3, is very small (≈0.002 eV) indicating weak coupling between the POR units due to the large distance between them (≈29 Å). In this system the charge distribution should be symmetrical in both POR fragments; however, any small change in the bond lengths or angles immediately breaks the symmetry and results in charge localization in one POR fragment as illustrated in Figure 9. The next LUMO + 4 level shows the charge distribution exclusively within the conjugated chain. Degenerate HOMO and HOMO − 1 levels belong to the POR parts of the dimer molecule (with the same illustration of charge localization at one POR fragment only due to the small splitting energy), while the next two degenerate HOMO − 2 and HOMO − 3 represent symmetrical and asymmetrical pairs of orbitals involving the entire dimer. Also in our calculations is the totally delocalized HOMO − 4 orbital. We conclude that the minimal number of orbitals required to model the POR dimer is eight, instead of four for the single POR. However, for a more detailed study, 10 MOs were considered including totally delocalized HOMO − 4 and LUMO + 4 with the charge distributed over the bridge-connector. Analysis of the energy-levels and transitions for the POR dimer provide insights into the nature of MOs with strong charge separation within the POR or chain parts exclusively. Corresponding transitions can also be localized at the particular molecular fragments. With this information and understanding of the POR dimer, we proceeded to calculations of the POR-SQU-POR macromolecule.

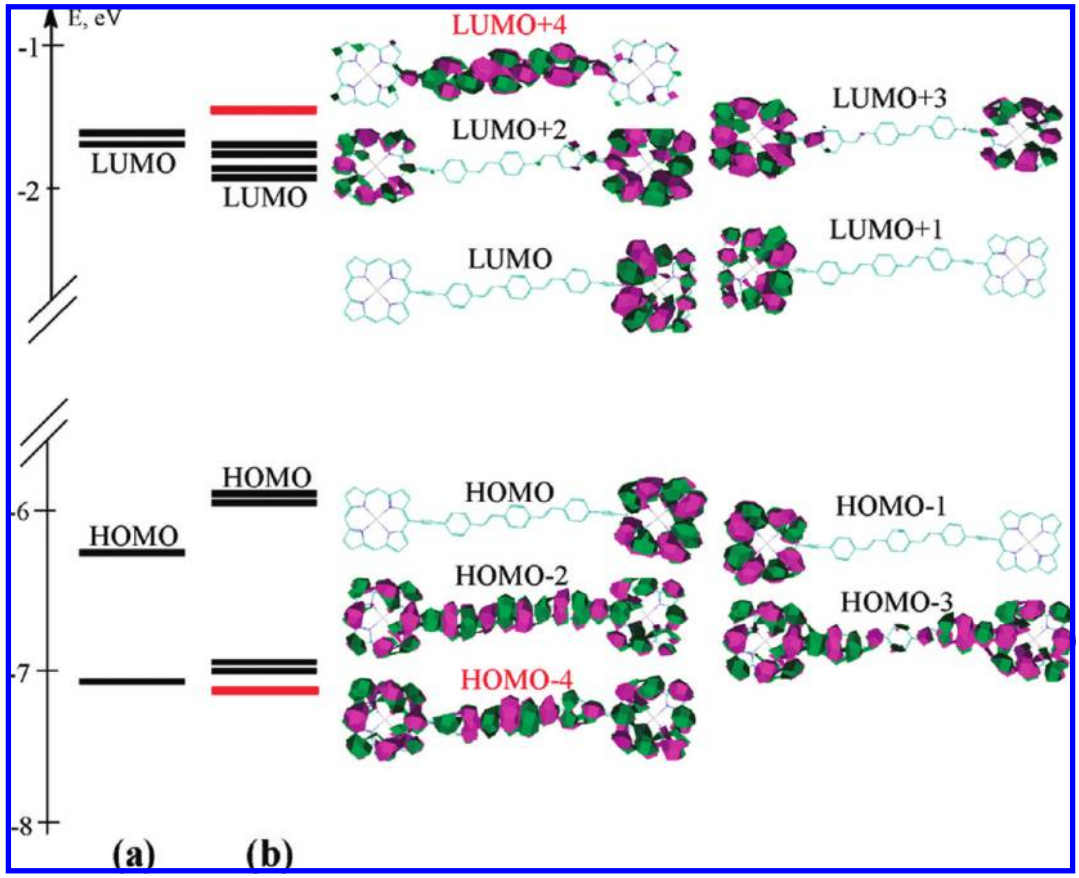

Figure 9. Schematic of molecular orbital energy-levels and charge density distribution for POR (a) and POR dimer (b). See Figure 7 for POR charge density distribution. Energy-levels within the POR fragments only and within the conjugated bridge only are shown in black and red, respectively.

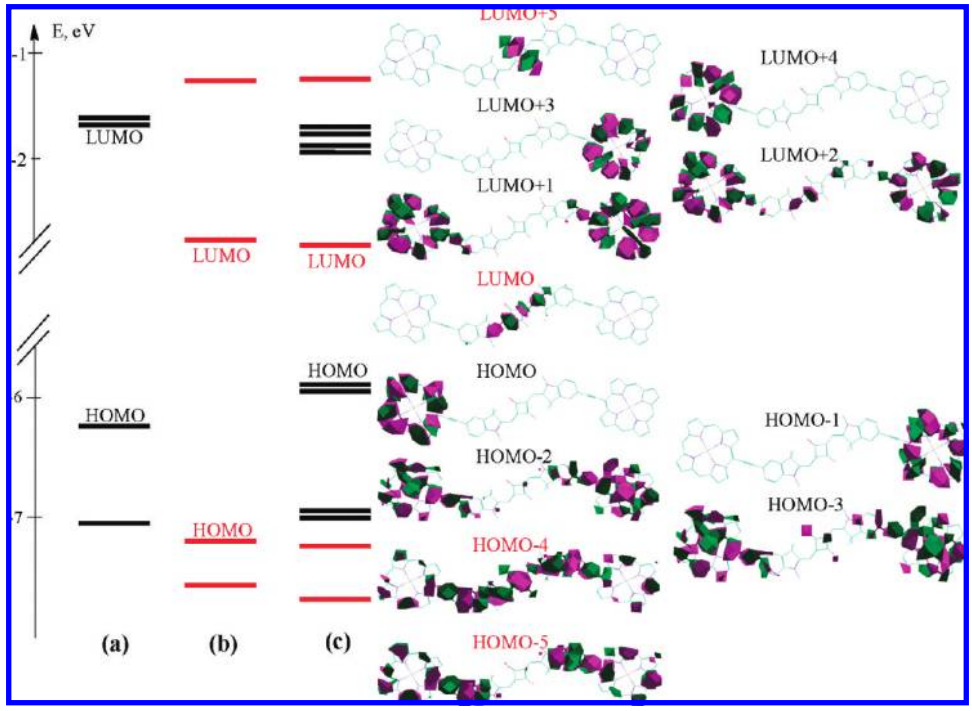

Figure 10. Schematic of the molecular orbital energy-levels and charge density distribution for POR (a), SQU (b), and POR-SQU-POR (c). In red are the energy-levels of the SQU molecule.

Figure 10 shows the energy-level diagram and charge density distributions for the POR-SQU-POR as compared to single POR and SQU molecules. From the calculations, there are three types of MOs, which differ in their charge distribution. The first type is connected with a charge localization at the POR fragments only and includes two pairs of degenerate occupied MOs—HOMO, HOMO − 1 and HOMO − 2, HOMO − 3 separated by a relatively large distance—and two pairs of degenerate unoc-

cupied MOs—LUMO + 1, LUMO + 2 and LUMO + 3, LUMO + 4 separated by a much smaller energy interval. Note that the main difference between these pairs is that for HOMO, HOMO − 1 and LUMO + 1, LUMO + 2, the coefficients $C_{i\mu} = 0$ for the atoms connecting the POR fragments with the conjugated chain lead to charge localization at POR constituents exclusively. For HOMO − 2, HOMO − 3 and LUMO + 3, LUMO + 4, the $C_{i\mu} \neq 0$ (for the same atoms) leads to charge slightly spreading to the chain connecting the POR fragments. The second type of MOs is exemplified by the molecular LUMO, which almost coincides with the LUMO of the SQU molecule. In the LUMO + 5, the charge is localized within the acceptor bridge of the SQU fragment and is oriented perpendicular to the conjugated chain. The third type of MOs, exemplified by the HOMO − 4 level, is delocalized over the entire molecule.

These properties of MOs are presumably responsible for the types of electronic transitions, which in turn, can be separated into three groups: electronic transitions within the POR fragments; transitions within the SQU bridge; and charge-transfer (CT) transitions from the POR to SQU fragments. Note that quantum-chemical calculation of the transition energies in POR-SQU-POR is a challenging task due to the different nature of its constituents. The transition energies in the POR fragments, as in other heterocyclic compounds, are characterized by relatively small distances between the atoms and can be satisfactory calculated with the Mataga−Nishimoto approximation, which is frequently used in semiempirical methods.[41] The transition energies in the SQU fragment, corresponding to the linearly conjugated system, can be satisfactorily calculated using the modified formulas proposed by Fabian and Zahradnic,[44] which take into account the potential field attenuation for the larger distances between atoms.[45] The main difficulty for calculation of the POR-SQU-POR is that the calibration of the transition energies in different molecular fragments should be different. Understanding the nature of the transitions plays a crucial role in our calculations.

Our calculations suggest that the first intense allowed $S_0 \rightarrow S_1$ transition is connected with electron transfer from the HOMO − 4, which is delocalized over both POR and SQU constituents, to the SQU-localized LUMO. Thus, this transition has both SQU-localized and POR-to-SQU CT character. Therefore, this transition in POR-SQU-POR is ≈100 nm red-shifted compared to that of the SQU molecule itself, due to the influence of the delocalized HOMO − 4 level. The next singlet transition, $S_0 \rightarrow S_2$, is connected with electron transfer from the HOMO (POR fragment) to LUMO (SQU fragment) and, thus, represents the first CT transition. The overlap integral between these two orbitals is negligible; therefore, this CT transition is not observed in the linear absorption spectrum and is only expected to be observable by 2PA, which is supported experimentally. The energetic position of the CT band almost coincides with the energy position of the $S_0 \rightarrow S_1$ band; therefore, the first 2PA band appears to be within the first linear absorption band. The next two transitions are connected with transitions within the POR fragments only and represent an almost unshifted POR Q-band. They are transitions from HOMO and HOMO − 1 to LUMO + 1 and LUMO + 2 (first part of the Q doublet) and from HOMO to LUMO + 3 and LUMO + 4 (second part of the Q doublet). The next two singlet transitions are connected with electron transfer from POR to SQU (from HOMO − 2 and HOMO − 3 to LUMO) and are the two next CT transitions, which are allowed in 2PA only. Finally, the next group of transitions corresponds to the B (or Soret) band of the POR part and is also unshifted as compared to the individual POR molecule. They are transitions from HOMO − 2 and HOMO − 3 to LUMO + 1 and LUMO + 2 (first part of the B doublet) and from HOMO − 2 and HOMO − 3 to LUMO + 3 and LUMO + 4 (second part of the B doublet). Transitions within the SQU part are at higher energies and presumably cannot be observed in the 350−850 nm spectral range. The excitation anisotropy spectrum is in excellent agreement with the quantum-chemical analysis: large and flat anisotropy values are seen within the $S_0 \rightarrow S_1$ band, analogous to the anisotropy seen for SQU, and extremes in the anisotropy function at 620, 550, 470, and 430 nm correspond to POR Q and B bands. In our preliminary communication, ref 27 and its Supporting Information, quantum chemical calculations and bond length optimizations were performed using the DFT/B3LYP level of theory using the 6-31G** basis set (TURBOMOLE package), and these support our conclusions that the broad and large 2PA from the POR-SQU-POR originate from several overlapping transitions which we identify as CT transitions from POR to SQU fragments.

Our study suggests that the prominent enhancement of the 2PA in POR-SQU-POR, as compared to its constituents, can be understood in terms of extended conjugated paths leading to a larger separation between the POR and SQU fragments as one might expect based upon the spectroscopy of the extended squaraine dyes[22] and porphyrin dimers.[46] However, a simple extension of the conjugation length does not necessarily lead to the broadening of the 2PA spectrum. Our understanding is that the main reason for such dramatic broadening of the 2PA spectrum, which covers the spectral range from 850 to 1600 nm (2PA scale) with two-photon cross sections ranging from 780 to 11 000 GM, is connected with efficient CT processes over the large distance from the POR to SQU constituents, facilitated by the alkyne bridges. An additional increase of δ_{2PA} from the 2PA wavelength of 950−850 nm is presumably connected with the enhancement in the POR dimer which may have a similar explanation as proposed in refs 8 and 46 and is confirmed by our quantum-chemical calculations.

We now analyze the nature and positions of the triplet states in the POR-SQU-POR molecule. As in the case of the singlet states, the triplet states are also connected with either POR or SQU constituents or both. The lowest triplet state T_1 is connected with the SQU part of the macromolecule and the splitting energy from the corresponding S_1 state, $\Delta E_{ST} \approx 0.6-0.7$ eV. This value is larger than in the POR molecule; however, it is much smaller than in the SQU itself, which explains the decrease in intersystem crossing rate as compared to POR and increase in comparison with SQU. The next, higher triplet states are connected with the POR parts of the macromolecule. Therefore, the probability of mixing between S_1 from the SQU unit with the triplet states belonging to the POR fragments is extremely low. It is interesting to compare our conclusions with the results for the POR dimer, where two porphyrin moieties are connected by a butadiene bridge. As shown in ref 47, the intersystem crossing yield for this dimer is 0.89; however, incorporation of a SQU molecule into the bridge changes the nature of the lowest singlet state resulting in the larger ΔE_{ST} value. These findings explain why the intersystem crossing yield for the POR-SQU-POR is only 0.025, as compared to 0.21 for POR and ≈0 for SQU (see Table 1).

4. Conclusions

We have described a detailed experimental investigation of the linear and nonlinear absorption properties of POR-SQU-POR in which two different classes of organic compounds, two

porphyrin heterocycles and a cyanine-like squaraine, are linked by conjugated bridges and have performed quantum-chemical analyses in order to understand the nature of the measured nonlinearities. All measured characteristics of the POR-SQU-POR macromolecule are compared with zinc porphyrin and squaraine constituents. The measurements were performed by femto-, pico-, and nanosecond laser pulses in order to obtain a reasonably complete picture of the intramolecular processes, obtain molecular parameters, and model the molecular dynamics. Experimental and quantum-chemical analyses allow us to make the following conclusions:

1. Electronic transitions within the POR-SQU-POR macromolecule can be separated into three groups: electronic transitions within the POR fragments; those within the SQU fragment; and intramolecular charge transfer transitions from the POR to SQU constituents. The first intense allowed $S_0 \rightarrow S_1$ transition is connected with electron transfer from the orbital totally delocalized over the entire macromolecule to the orbital connected with the SQU part only. This transition, having characteristics of the SQU absorption band, is, however, $\approx$100 nm red-shifted due to the delocalized orbital. The next $S_0 \rightarrow S_2$ transition, forbidden by symmetry in 1PA, is connected with electron transfer from the POR to SQU fragment and is the first CT transition observed in the 2PA spectrum. The energy of this CT band coincides with that of the $S_0 \rightarrow S_1$ band; therefore, this 2PA band is found to be within the first absorption band. The following two transitions, represented by the doublet with two nearly orthogonal dipole moments, are related to the almost unshifted POR Q-band and are clearly observed in the linear absorption spectrum. The next two transitions are associated with CT from the POR to SQU part and are allowed in 2PA only. The high-energy doublet corresponding to the B (or Soret) band of the POR fragments is also unshifted as compared to the initial POR molecule.

2. Compared to its constituent parts, the broad 2PA spectrum (spectral range from 850 to 1600 nm) and strong enhancement of δ_{2PA} in POR-SQU-POR can be explained by the existence of several efficient CT bands across the large planar conjugated path via alkyne triple bonds from the POR to the SQU constituents.

3. The differences in intersystem crossing yields of the porphyrin (0.21), squaraine ($\approx$0), and POR-SQU-POR (0.025) can be explained by the different splitting energies between the first excited singlet and triplet states: the smallest in the porphyrin and the largest in the squaraine molecule.

These well-known and studied chromophores have been linked together resulting in increased 2PA cross sections, compared to its constituents, across an unprecedented long wavelength range covering most of the near-infrared. Although the triplet yield, and hence long-lived excited-state was not enhanced as expected, we are working on combining other chromophores and engineering their structures to create molecular systems with large 2PA cross sections, long-lived excited-state absorptions, and strong nonlinear responses from the visible to near-infrared wavelength region.

Acknowledgment. We gratefully acknowledge the support of the National Science Foundation ECS 0524533, the US Army Research Laboratory W911NF0420012, the US Army Research Laboratory and the US Army Research Office under Contract/Grant Number 50372-CHMUR, and the Office of Naval Research MORPH N00014-06-1-0897. S.A.O. acknowledges support from an NSF Graduate Research fellowship. H.L.A. and S.A.O. acknowledge support from the Engineering and Physical Sciences Research Council (EPSRC).

References and Notes

(1) Gouterman, M. *J. Chem. Phys.* **1960**, *33*, 1523.
(2) Gouterman, M. In *The Porphyrins*; Dolphin, D., Ed.; Academic Press: New York, 1978; Vol. 3, Chapter 1.
(3) Baerends, E. J.; Ricciardi, G.; Rosa, A.; Van Gisbergen, S. J. A. *Coord. Chem. Rev.* **2002**, *230*, 5.
(4) Nguyen, K. A.; Pachter, R. *J. Chem. Phys.* **2001**, *114*, 10757.
(5) Liao, M.-S.; Scheiner, S. *J. Chem. Phys.* **2002**, *117*, 205.
(6) Blau, W.; Byrne, H.; Dennis, W.; Kelly, J. *Opt. Commun.* **1985**, *56*, 25.
(7) Rubio-Pons, O.; Luo, Y.; Agren, H. *J. Chem. Phys.* **2006**, *124*, 094310/1.
(8) Drobizhev, M.; Stepanenko, Y.; Dzenis, Y.; Karotki, A.; Rebane, A.; Taylor, P. N.; Anderson, H. L. *J. Am. Chem. Soc.* **2004**, *126*, 15352.
(9) Ray, P. C.; Sainudeen, Z. *J. Phys. Chem. A* **2006**, *110*, 12342.
(10) Kawatta, S.; Kawatta, Y. *Chem. Rev.* **2000**, *100*, 1777.
(11) Calvete, M.; Yang, G. Y.; Hanack, M. *Synth. Met.* **2004**, *141*, 231.
(12) Walters, V. A.; de Paula, J. C.; Jackson, B.; Hall, K.; Lind, J.; Cardozo, K.; Chandran, K.; Raible, D.; Phillips, C. M. *J. Phys. Chem.* **1995**, *99*, 1166.
(13) Mansour, K.; Alvarez, D.; Perry, K.; Choong, I.; Marder, S.; Perry, J. *Proc. SPIE* **1993**, *1853*, 132.
(14) Kim, Y. H.; Cho, H. S.; Kim, D.; Kim, S. K.; Yoshida, N.; Osuka, A. *Synth. Met.* **2001**, *117*, 183.
(15) Cho, H. S.; Jeong, D. H.; Cho, S.; Kim, D.; Matsuzaki, Y.; Tanaka, K.; Tsuda, A.; Osuka, A. *J. Am. Chem. Soc.* **2002**, *124*, 14642.
(16) Collins, H. A.; Khurana, M.; Moriyama, E. H.; Mariampillai, A.; Dahlstedt, E.; Balaz, M.; Kuimova, M. K.; Drobizhev, M.; Yang, V. X. D.; Phillips, D.; Rebane, A.; Wilson, B. C.; Anderson, H. L. *Nat. Photonics* **2008**, *2*, 420.
(17) Pawlicki, M.; Collins, H. A.; Denning, R. G.; Anderson, H. L. *Angew. Chem., Int. Ed.* **2009**, *48*, 3244.
(18) Kim, K. S.; Lim, J. M.; Osuka, A.; Kim, D. *J. Photochem. Photobio. C* **2008**, *9*, 13.
(19) Fu, J.; Przhonska, O. V.; Padilha, L. A.; Hagan, D. J.; Van Stryland, E. W.; Bondar, M. V.; Slominsky, Yu.L.; Kachkovski, A. D. *J. Opt. Soc. Am. B* **2007**, *24*, 56.
(20) Fu, J.; Padilha, L. A.; Hagan, D. J.; Van Stryland, E. W.; Przhonska, O. V.; Bondar, M. V.; Slominsky, Yu.L.; Kachkovski, A. D. *J. Opt. Soc. Am. B* **2007**, *24*, 67.
(21) Lepkowicz, R. S.; Przhonska, O. V.; Hales, J. M.; Hagan, D. J.; Van Stryland, E. W.; Bondar, M. V.; Slominsky, Yu. L.; Kachkovski, A. D. *J. Opt. Soc. Am. B* **2005**, *22*, 2664.
(22) Chung, S. J. *J. Am. Chem. Soc.* **2006**, *128* (45), 14444.
(23) Scherer, D.; Dörfler, R.; Feldner, A.; Vogtmann, T.; Schwoerer, M.; Lawrentz, U.; Grahn, W.; Lambert, C. *Chem. Phys.* **2002**, *279*, 179.
(24) Terenziani, F.; Painelli, A.; Katan, C.; Charlot, M.; Blanchard-Desce, M. *J. Am. Chem. Soc.* **2006**, *128*, 15742.
(25) Lim, J. H.; Przhonska, O. V.; Khodja, S.; Yang, S.; Ross, T. S.; Hagan, D. J.; Van Stryland, E. W.; Bondar, M. V.; Slominsky, Yu. L. *Chem. Phys.* **1999**, *245*, 79.
(26) Webster, S.; Reyes-Reyes, M.; Pedron, X.; Lopez-Sandoval, R.; Terrones, M.; Carroll, D. L. *Adv. Mater.* **2005**, *7*, 1239.
(27) Odom, S. A.; Websterzfn, S.; Padilha, L. A.; Peceli, D.; Hu, H.; Nootz, G.; Chung, S.-J.; Ohira, S.; Matichak, J. D.; Przhonska, O. V.; Kachkovski, A. D.; Barlow, S.; Brédas, J.-L.; Anderson, H. L.; Hagan, D. J.; Van Stryland, E. W.; Marder, S. R. *J. Am. Chem. Soc.* **2009**, *131*, 7510.
(28) Magde, D.; Brannon, J. H.; Cremers, T. L.; Olmsted, J. *J. Phys. Chem.* **1979**, *83*, 696.
(29) Strickler, S. J.; Berg, R. A. *J. Chem. Phys.* **1962**, *37* (4), 814.
(30) Lakowicz, J. R. In *Principles of fluorescence spectroscopy*, second ed.; Kluwer Academic/Plenum Publishers: New York, 1999.
(31) Webster, S.; Fu, J.; Padilha, L.; Przhonska, O. V.; Hagan, D. J.; Van Stryland, E. W.; Bondar, M. V.; Slominsky, Yu. L.; Kachkovski, A. D. *Chem. Phys.* **2008**, *348*, 143.
(32) Karolczak, J.; Kowalska, D.; Lukaszewicz, A.; Maciejewski, A.; Steer, R. P. *J. Phys. Chem. A* **2004**, *108* (21), 4570.
(33) Sheik-Bahae, M.; Said, A. A.; Van Stryland, E. W. *Opt. Lett.* **1989**, *14*, 955.
(34) Xu, C.; Webb, W. W. *J. Opt. Soc. Am. B* **1996**, *13*, 481.
(35) Sheik-Bahae, M.; Said, A. A.; Wei, T.-H.; Hagan, D. J.; Van Stryland, E. W. *IEEE J. Quant. Electron.* **1990**, *26*, 760.
(36) Lepkowicz, R. S.; Przhonska, O. V.; Hales, J. M.; Fu, J.; Hagan, D. J.; Van Stryland, E. W.; Bondar, M. V.; Slominsky, Yu.L.; Kachkovski, A. D. *Chem. Phys.* **2004**, *305*, 259.

(37) Swatton, S. R.; Welford, K. R.; Hollins, R. C.; Sambles, J. R. *Appl. Phys. Lett.* **1997**, *71*, 10.

(38) He, G. S.; Zheng, Q.; Baev, A.; Prasad, P. N. *J. Appl. Phys.* **2007**, *101*, 083108/1.

(39) Schroeder, R.; Ullrich, B. *Opt. Lett.* **2002**, *27*, 1285.

(40) Padilha, L. A.; Webster, S.; Hua, H.; Przhonska, O. V.; Hagan, D. J.; Van Stryland, E. W.; Bondar, M. V.; Davydenko, I. G.; Slominsky, Yu.L.; Kachkovski, A. D. *Chem. Phys.* **2008**, *352*, 97.

(41) Zerner, M. C.; Loew, G. H.; Kirchner, R. F.; Mueller-Westerhoff, U. T. *J. Am. Chem. Soc.* **1980**, *102*, 589.

(42) Dewar, M. J. S. *The Molecular Orbital Theory of Organic Chemistry*; McGraw-Hill: New York, 1969.

(43) Nguyen, K. A.; Day, P. N.; Pachter, R. *J. Chem. Phys. A* **1999**, *103*, 9378.

(44) Fabian, J.; Zahradnik., R.; Wiss, Z. *Techn. Univ. (Dresden)* **1977**, *26*, 315.

(45) Tyutyulkov, N.; Gochev, A.; Fratev, F. *Chem. Phys. Lett.* **1969**, *4*, 9.

(46) Drobizhev, M.; Stepanenko, Y.; Dzenis, Y.; Karotki, A.; Rebane, A.; Taylor, P. N.; Anderson, H. L. *J. Phys. Chem. B* **2005**, *109*, 7223.

(47) Kuimova, M. K.; Collins, H. A.; Balaz, M.; Dahlstedt, E.; Levitt, J. A.; Sergent, N.; Suhling, K.; Drobizhev, M.; Makarov, N. S.; Rebane, A.; Anderson, H. L.; Phillips, D. *Org. Biomol. Chem.* **2009**, *7*, 889.

JP904460F